

# Mechanistic framework for deriving reduced-order models in soft materials: Application to granular intrusion

Shashank Agarwal<sup>a</sup>, Daniel I Goldman<sup>b</sup>, and Ken Kamrin<sup>a</sup>

<sup>a</sup>Department of Mechanical Engineering, Massachusetts Institute of Technology, Cambridge; <sup>b</sup>Department of Physics, Georgia Institute of Technology, Atlanta

This manuscript was compiled on August 19, 2022

**Soft materials often display complex behaviors that transition through apparent solid- and fluid-like regimes. While a growing number of microscale simulation methods exist for these materials, reduced-order models that encapsulate the global-scale physics are often desired to predict how external bodies interact with soft media, as occurs in diverse situations from impact and penetration problems to locomotion over natural terrains. This work proposes a systematic program to develop three-dimensional reduced-order models for soft materials from a fundamental basis using continuum symmetries and rheological principles. In particular, we derive a reduced-order technique for modeling intrusion in granular media which we term three-dimensional Resistive Force Theory (3D-RFT), which is capable of accurately and quickly predicting the resistive stress distribution on arbitrary-shaped intruding bodies. Aided by a continuum description of the granular medium, a comprehensive set of spatial symmetry constraints, and a limited amount of reference data, we develop a self-consistent and accurate 3D-RFT. We verify the model capabilities in a wide range of cases and show it can be quickly recalibrated to different media and intruder surface types. The premises leading to 3D-RFT anticipate application to other soft materials with strongly hyperlocalized intrusion behavior.**

Soft matter | Intrusion modeling | Resistive Force Theory | Continuum modeling | Granular media

Intrusion in soft media is a common occurrence in nature arising in biological and vehicular locomotion, excavation and anchoring applications, and meteorite and ballistic impact problems (1–4). Modeling intrusion in real-time is critical for a variety of applications and would enable heuristic understanding and quick insight into phenomena like biological circummutation (5) and robot-terrain interactions (6). But the multiphase nature of these materials — simultaneous solid- and fluid-like behaviors (7) — makes modeling such systems computationally challenging. In the specific case of granular media, despite over a century of progress in the disciplines of granular physics and *terramechanics* — the study of the interaction of tracked vehicles on various substrates (8) — challenges remain. Many commonly used methods have limited applicability due to their shape- or media-specific nature. For instance, commonly used terramechanical empirical models such as the Bekker model (9) (later modified by Wong and Reece (10)) and Magic formulae (11) are limited to specific geometries such as circular wheels. Inspired by an analogous approach for viscous fluids (12, 13), in recent years a granular Resistive Force Theory (RFT) has been introduced (14) to model the forces on arbitrarily shaped intruders in granular media, but its form is limited to 2-dimensional problems. This poses limits on its usage in many practical applications. At-

tempts to extend RFT to 3D intruders have only recently been explored based on empirical fitting, though these approaches have known limitations (5, 15) (see Sec 1 of Supplemental Information for comparison and critique).

While granular intrusions represent a wide class of intrusion problems, equally plentiful problems exist in other soft material systems such as muds and slurries. The challenges are further exacerbated by the 3-dimensional nature of such problems that require additional physical self-consistency constraints. Thus, this work introduces a generic program for developing intrusion models in a wide class of soft materials and exemplifies its use in the case of granular media. The basic program is to combine three ingredients from the full-field physics of the soft media to extract a “hyper-localized” rule-set for determining intrusive stresses. First, a continuum model that parsimoniously represents the rheology of the media is identified. Second, dimensional analysis of the continuum system together with surface-media boundary stress constraints are used to obtain a generic functional form for the local intrusion stress formula. Third, global symmetries are enforced to reduce the remaining functional dependences. In our application to granular intrusions herein, the final step is to fill in the remaining details of the resulting functions using a targeted set of in-silico reference tests. We use this program to develop a 3D-RFT model with additional efforts to keep its structure similar to the previous 2D-RFT. We test the 3D-RFT model against a variety of granular intrusions, consisting of the arbitrary motion of many symmetric and asymmetric shapes in beds of granular media. We find excellent agreement between the reference results and 3D-RFT predictions both globally (total intrusion force and moment) and locally (surface stress distribution). Thus, the proposed set of steps, which could also be extended to other soft flowable

## Significance Statement

This work proposes a general theory for modeling diverse granular intrusion problems such as animal and human locomotion in sands and other natural terrains. Respecting numerous physical constraints, the theory allows for modeling arbitrary motion of three-dimensional generally-shaped objects in granular media in near real-time. Moreover, the work provides a generic mechanistic framework for developing self-consistent physics-informed reduced-order models for a wider class of soft materials.

<sup>2</sup>To whom correspondence should be addressed. E-mail: kkamrin@mit.edu

materials, helps us develop a 3D-RFT framework that satisfies all needed physical constraints, is robust and predictive, and whose dependence on material parameters and surface roughnesses is transparent.

## 1. Review of existing RFT

The Resistive Force Theory methodology was originally introduced by Gray and Hancock (12) for modeling self-propelling undulatory biological systems in viscous fluids. In this model, a simple approximate formula for the resistive force on a segment of a thin body is derived from the Stokes equations as a function of the segment's velocity components, orientation, and a few variables characterizing the fluid-segment interaction. Importantly, the theory assumes decoupling of the forces over the various segments of the body (13). The success of fluid RFT motivated multiple studies (14, 16, 17) to explore the existence of a similar theory in granular media.

Li et al (14) proposed a planar (or 2-dimensional) version of RFT for dry granular media (2D-RFT). In 2D-RFT, at low-speeds, the rate-independent nature of granular media (characterized by low values of the non-dimensional (micro-) inertial number  $I$  (18–20) and macro-inertial number  $I_{\text{mac}}$ , see Materials and Methods) makes the dependence of intrusion force independent of the velocity magnitude. Assuming material strength increases with pressure and that pressure is primarily due to gravity, Li's 2D-RFT model has the following form:

$$\mathbf{F}^{\text{total}} = \int_{\text{surf}} (\alpha_x(\beta, \gamma), \alpha_z(\beta, \gamma)) |z| ds. \quad [1]$$

Here,  $\mathbf{F}^{\text{total}}$  represents the total force on an intruding surface, which is divided into smaller planar sub-surface elements of area  $ds$  and depth  $|z|$  from the free surface. The *tilt angle*  $\beta$  and *angle of attack*  $\gamma$  characterize the orientation and motion of each surface element of the intruding body (see Fig 1)A. The vector-valued function of angles  $\alpha = (\alpha_x, \alpha_z)$  represents the force per unit area per unit depth; this function must be obtained a priori through experiments or simulations of plate drag and depends on the material properties of the granular media, the intruder surface interaction, and the value of gravity. Of note, Eq 1 assumes no correlation between the forces on different sub-surfaces; only details local to a surface element determine the force on that element (16). A comprehensive comparison of various existing reduced order methods for modeling granular intrusions, including 2D-RFT and a *terramechanical* model, can be referred from Agarwal et al. (2).

In recent years, it has been shown that plasticity-based PDE models can also obtain the form of 2D granular RFT (21). More recently, the performance of the continuum approach in modeling a variety of granular intrusions has been demonstrated for wheeled locomotion, impact and penetration, and multi-body intrusion (2, 22–25). Additionally, the approach also provides insight into the somewhat surprising observation that granular RFT is often more accurate than its viscous fluid counterpart (12, 13). Thus, while experimental observations primarily drove the original RFT discoveries, the availability of faster computational methods, the success of 2D-RFT, and a need for better real-time 3D granular intrusion methods have driven the exploration of 3D-RFT. Our work combines the capabilities of the continuum approach with a

few symmetry requirements and DEM data to accurately and efficiently model the physics of 3-dimensional granular intrusion to develop a 3D-RFT based on our proposed mechanistic framework. We briefly discuss the details of the continuum approach next.

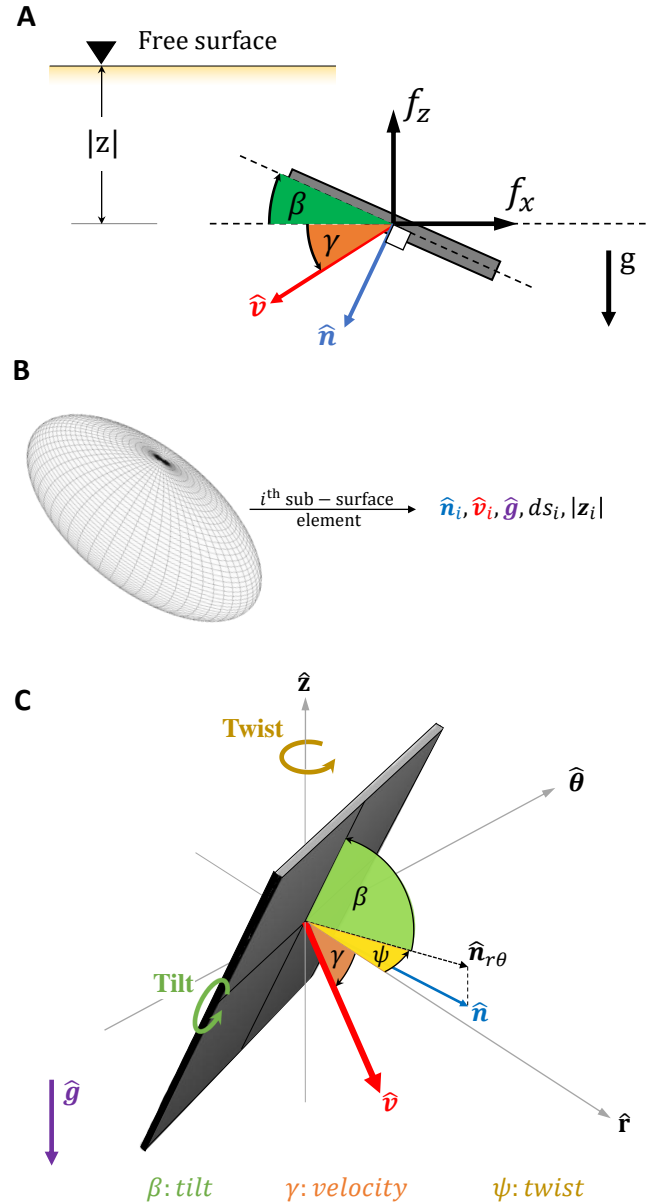


**Fig. 1. 2D RFT sub-surface characterization:** Any moving sub-surface is represented using a set of two characteristic angles — plate tilt ( $\beta$ , green) and angle of attack ( $\gamma$ , orange). **3D-RFT surface element characterization:** (A) Any moving sub-surface is represented using surface normal ( $\hat{n}$ ), area magnitude ( $ds$ ), depth ( $|z|$ ), velocity direction ( $\hat{v}$ ), and gravity direction ( $\hat{g}$ ). (B) Directions  $\hat{n}$  and  $\hat{v}$  are expressed using three characteristic angles — plate tilt ( $\beta$ , green), plate twist ( $\psi$ , yellow), and velocity angle ( $\gamma$ , orange) in the local coordinate frame  $\{\hat{r}, \hat{\theta}, \hat{z}\}$ .

## 2. Guidance from continuum modeling

We use continuum modeling as the primary theoretical motivator as well as a reference data generation tool in this work. The constitutive model we use (22, 23) has a response characterized

by a rate-insensitive, non-dilatant frictional flow rule when in a dense state, but also models the separated state which allows material to become stress-free when below a *critical density*. The model has been validated in a number of previous studies of granular intrusion and locomotion (21, 25–28).

The constitutive flow equations representing the material's separation behavior, shear yield condition, and tensorial co-directionality, respectively, are shown below:

$$\begin{aligned} (\rho - \rho_c)P &= 0 & \text{and } P &\geq 0 & \text{and } \rho &\leq \rho_c, \\ \dot{\gamma}(\tau - \mu_{\text{int}}P) &= 0 & \text{and } \dot{\gamma} &\geq 0 & \text{and } \tau &\leq \mu_{\text{int}}P, \\ D_{ij}/\dot{\gamma} &= \sigma'_{ij}/2\tau & \text{if } \dot{\gamma} &> 0 & \text{and } P &> 0 \end{aligned} \quad [2]$$

where,  $i, j = 1, 2, 3$ . In these equations,  $\boldsymbol{\sigma}$  represents the Cauchy stress tensor and  $\sigma'_{ij} = \sigma_{ij} + P\delta_{ij}$  represents the deviatoric part of  $\boldsymbol{\sigma}$  where  $P = -\sigma_{ii}/3$  represents the hydrostatic pressure.  $\tau = \sqrt{\sigma'_{ij}\sigma'_{ij}}/2$  represents the equivalent shear stress and  $\mu_{\text{int}}$  and  $\rho_c$  represent the constant bulk friction coefficient and critical close-packed density of the granular media.  $D_{ij} = (\partial_i v_j + \partial_j v_i)/2$  represents the (plastic) flow rate tensor, and  $\dot{\gamma} = \sqrt{2D_{ij}D_{ij}}$  represents the equivalent shear rate. We assume the surface friction coefficient  $\mu_{\text{surf}}$ , which is maximal for fully-rough surfaces where  $\mu_{\text{surf}} = \mu_{\text{int}}$ , describes the interaction of the granular continuum with intruder surfaces.

We use a 3D Material Point Method (MPM) solver from Baumgarten and Kamrin (29) to implement the continuum modeling in this study, which has been successfully used for modeling complex problems in the past (29, 30). We have also validated the accuracy of the continuum model against experiments for a specific set of 3D plate intrusions, which justify the use of the continuum solver for generating 3D-RFT reference data in the final step of the model development. The details of the validation studies are provided in the Methods and Materials section.

### 3. Proposed procedure: Physically-constrained intrusion modeling

We begin by discussing a three-step procedure which can be used to infer reduced-order intrusion models in soft media. This is followed by a derivation in Sec 4 showing how these ingredients are used to deduce 3D-RFT in granular media.

*Step-1: Order-reduction hypothesis.* We assume that the intrusion stress on each surface element of the intruder is approximately equal to that of an isolated plate element in the same configuration moving the same way. This is the key order-reduction hypothesis in the RFT family of models, though other reductive hypotheses could conceivably be used.

*Step-2: Apply constraints from continuum description.* The previous step reduces the problem to inferring a force relation on isolated plate elements. We now identify a continuum model for the media and use it to impose constraints on the intrusion force relation as implied by the continuum system. These constraints can be inferred through dimensional analysis of the model parameters and through analysis of stress state limitations in the rheology and boundary conditions.

*Step-3: Apply global symmetry constraints.* Any function providing the intrusion force on an intruder must obey a

symmetry relationship whereby if the entire problem is rotated by some amount — that is the free-surface, gravity, intruder orientation/position, and intruder velocity are all rotated the same amount — then the resistive force must also rotate by this common global rotation. As we will show, this constraint, which implies the drag force relations are isotropic functions of their inputs, imposes a rather strong restriction on the three-dimensional form that 3D-RFT can take.

It is only after Steps 1-3 have reduced down the functional form of the intrusion model considerably that we then refer to data to fit the remaining details. Of key importance, much less fitting must be done and one is assured the result obeys basic physical principles when the above procedure is used. As we shall show with 3D-RFT, this procedure results in an accurate model with an explicit dependence on material parameters that can be exploited to enable rapid calibration to various granular media.

In the case of granular 3D-RFT, the execution of Step 2 uses the continuum model discussed previously and summarized in Eq 2. Assuming the continuum model holds, the resistive force on a surface element depends on the same limited set of material parameters that govern the continuum model:  $\rho_c$  (the critical density),  $\mu_{\text{int}}$  (the internal friction), and  $\mu_{\text{surf}}$  (the media-surface friction). This requirement is quite constraining when combined with dimensional analysis. Also, the continuum model's lack of tensile stress states is enforced by requiring resistive stress to only have positive compressive normal component and to occur only on *leading edges* of the intruder. That is, only surfaces moving 'into' and not 'away from' a granular volume experience non-negligible resistive force. Section S7 in the Supplementary Information provides evidence in support of this hypothesis in three dimensions. The continuum model's boundary conditions also come to use. Since the intruder is assumed to have a surface-media friction coefficient  $\mu_{\text{surf}}$ , the ratio of tangential and normal stress on a surface element cannot exceed this value. In agreement with this requirement, we observe in extensive analysis of continuum model solutions that plate-tangential resistive forces generated at a higher  $\mu_{\text{surf}}$  can be used to generate the tangential force for a lower  $\mu_{\text{surf}}$  by simply limiting the magnitude of the tangential force based on the Coulomb friction limit. Detailed material response graphs in this regard can be found in Sec S5 of the Supplementary Information. Our extensive data analysis also allows us to assert that the normal force is relatively uninfluenced by  $\mu_{\text{surf}}$  for a large range of internal friction ( $\mu_{\text{int}} = 0.3 - 0.9$ ) (see Fig S2). Between different  $\mu_{\text{int}}$ , the normal forces appear to only vary by a multiplicative scalar factor  $\xi_n$  as discussed in Sec 4.

In addition to these premises, we will utilize a few operational constraints. We desire a 3D-RFT model that collapses back to the previously defined 2D-RFT description in the appropriate limits. Thus, we desire to ultimately express 3D-RFT in terms of similar characteristic angles  $\beta$  and  $\gamma$  and a new twist angle  $\psi$  representing the angle between the planes of plate normal and velocity direction with the vertical, similar to the angle-based characterization of 2D-RFT by Li et al. (14) (Fig 1)A. Also, we limit ourselves to quasi-static intruder motions, with negligible inertial effects in the granular media. This was also assumed in the original 2D-RFT formulation and lets the force on a sub-surface be deemed independent

of the surface's speed. More recently, an inertia-sensitive 2D-RFT has also been proposed and validated (25). We limit our attention to quasi-static cases in this work (See Materials and Methods section for more details). We also require that intruders are only submerged to a shallow depth. This requirement comes from the limit on the linearity of granular material's resistance with depth  $|z|$  in a gravity-loaded system and limits us to considering depths only up to a  $O(1)$  factor of the size of the object being intruded (24, 31). Lastly, the RFT form assumes grains to be small relative to the size-scale of the intruder. RFT is expected to have reduced accuracy along intruder surfaces that sharply vary; direct grain-size effects may be important to determining the resistive force on these subsurfaces.

#### 4. Deducing physically-constrained 3D-RFT

We use the previously discussed steps to propose a general form of the intended 3D-RFT model. In light of Step 1, we propose a 3D-RFT that supposes the force on any small surface element of the intruding body is equal to what the force would be if the plate element were isolated and moving on its own. Hence, the force (per area per depth,  $\alpha$ ) is a function that depends only on the element's surface normal  $\hat{n}$ , local velocity direction  $\hat{v}$ , and depth  $|z|$ , along with the acceleration of gravity  $\mathbf{g}$  and material properties 'mat', such that the total intrusion force satisfies

$$\mathbf{F}^{\text{total}} = \int_{\text{surf}} \alpha(\hat{n}, \hat{v}, \mathbf{g}, |z|; \text{mat}) |z| ds. \quad [3]$$

Referring to Step 2, the material properties are taken to be given by the parameter set  $\text{mat} = \{\rho_c, \mu_{\text{int}}, \mu_{\text{surf}}\}$ . Assuming for the time being that the intruder is fully rough,  $\mu_{\text{surf}} = \mu_{\text{int}}$ , dimensional analysis together with the observed dependence on  $\mu_{\text{int}}$  in Fig S2 reduces the functional dependence of  $\alpha$  significantly, requiring that

$$\alpha = \rho_c g \hat{f}(\mu_{\text{int}}) \alpha^{\text{gen}}(\hat{n}, \hat{v}, \hat{g}) \quad [4]$$

where  $\mathbf{g} = g\hat{g}$ , the dimensionless function  $\hat{f}$  is as-yet undetermined, and the prefactor  $\rho_c g \hat{f}(\mu_{\text{int}})$ , which we collectively refer to as  $\xi_n$ , is a media dependent scaling coefficient reflecting the overall intrusive strength of the system. The *generic* RFT function  $\alpha^{\text{gen}}$  is labeled as such because, under the given premises, it is universal across all granular/intruder systems with fully-rough interfaces.

We can uniquely decompose the vector-valued function  $\alpha^{\text{gen}}$  into normal and tangential directions as  $\alpha^{\text{gen}} \equiv \alpha_n^{\text{gen}} + \alpha_t^{\text{gen}}$ . We may now remove the fully-rough assumption and suppose  $\mu_{\text{surf}} \neq \mu_{\text{int}}$ . Then, in accord with the surface friction limit and Sec S5, we can simply scale down the tangential component of surface stress based on the surface friction limit by writing

$$\alpha = \rho_c g \hat{f}(\mu_{\text{int}}) \left[ \alpha_n^{\text{gen}} + \min \left( \frac{\mu_{\text{surf}} |\alpha_n^{\text{gen}}|}{|\alpha_t^{\text{gen}}|}, 1 \right) \alpha_t^{\text{gen}} \right]. \quad [5]$$

The 3D-RFT model we are proposing is closed upon choosing the scalar-valued function  $\hat{f}(\mu_{\text{int}})$  and the vector valued function  $\alpha^{\text{gen}}(\hat{n}, \hat{v}, \hat{g})$ . Upon selection of these two functions, Eq 5 can be used to determine  $\alpha$  for any choice of material and interface properties  $\{\rho_c, \mu_{\text{int}}, \mu_{\text{surf}}\}$ .

We now apply symmetry constraints inherent to the drag problem (Step 3) to further constrain the functional form

of  $\alpha^{\text{gen}}$ . Our strategy is to constrain the function space to satisfy symmetry constraints *by design* rather than leaving it to chance based on the choice of fit functions. Moreover, by enforcing the symmetry constraints directly, we reduce the space of admissible functions, thereby reducing the amount of fitting that must be done.

Consider a small plate intruder characterized with  $\hat{n}$ ,  $\hat{v}$ ,  $ds$ ,  $|z|$ , and  $\mathbf{g}$ . For  $\mu_{\text{surf}} = \mu_{\text{int}}$ , the force on the plate according to RFT is  $d\mathbf{f} = \xi_n \alpha^{\text{gen}}(\hat{n}, \hat{v}, \mathbf{g}) |z| ds$ . If the entire system is rotated including the intruder, the granular bed, and gravity the resistive force on the intruder must rotate by the same amount. This is because rotating the entire system should be consistent with a fixed system and a rotation of the observer. Figure 2A visualizes this action. Thus, for any rotation  $\mathbf{R}$ , we expect that  $\mathbf{R} d\mathbf{f} = \xi_n \alpha^{\text{gen}}(\mathbf{R}\hat{n}, \mathbf{R}\hat{v}, \mathbf{R}\hat{g}) |z| ds$ , and thus

$$\alpha^{\text{gen}}(\mathbf{R}\hat{n}, \mathbf{R}\hat{v}, \mathbf{R}\hat{g}) = \mathbf{R} \alpha^{\text{gen}}(\hat{n}, \hat{v}, \hat{g}). \quad [6]$$

This '*global rotation constraint*' implies  $\alpha^{\text{gen}}$  is an isotropic function of its inputs. Thus, in accord with Isotropic Representation Theory (IRT)(33) the function must have the following specific form:

$$\alpha^{\text{gen}}(\hat{n}, \hat{v}, \hat{g}) = f_1 \hat{n} + f_2 \hat{v} + f_3 \hat{g}, \quad [7]$$

where  $f_1$ ,  $f_2$ , and  $f_3$  are three mutually-independent arbitrary scalar-valued functions of coordinate-invariant *dot-products* between the three direction vectors, that is  $f_i = f_i(\hat{g} \cdot \hat{v}, \hat{g} \cdot \hat{n}, \hat{n} \cdot \hat{v})$ . Equation 7 has reduced the problem of fitting  $\alpha^{\text{gen}}$  from determining a vector-valued function of six independent variables (three vectors, each with a constraint of being unit magnitude) to determining a vector-valued function of three independent variables (three dot products). Note that the form given in Eq 5 for general  $\mu_{\text{surf}}$  continues to satisfy the IRT requirement Eq 7. A detailed proof in this regard is provided in section S6 of the Supplementary Information.

We next introduce the methodology for parametrizing sub-surfaces in terms of three angles to arrive at our ultimate description of  $\alpha^{\text{gen}}$ .

**3D-RFT sub-surface characterization.** Equation 7 defines the normalized stress-per-depth on a sub-surface using  $\hat{n}$ ,  $\hat{v}$ , and  $\hat{g}$  directions and corresponding dot products. We could stop here and set out to fit the  $f_i$  functions, however, there are certain advantages to first re-expressing Eq 7 in terms of an orthogonal set of directions and angles measured from those directions. Using angles helps us meet our desire to maintain a consistency of 3D-RFT with the 2D-RFT form, which is also angle-based, and using an orthogonal basis rather than  $\{\hat{n}, \hat{v}, \hat{g}\}$  eases the physical interpretation and simplifies calibration.

We define a local cylindrical coordinate system at each surface element as follows (see Fig 1C): We choose the direction opposite to the gravity (upward in general) as the positive  $z$ -direction and use the horizontal component of  $\hat{v}$  as the positive  $\hat{r}$  direction. The remaining  $\hat{\theta}$  direction is chosen as the cross product between  $\hat{r}$  and  $\hat{z}$ . The free-surface is taken as the reference ( $z = 0$ ) for the  $z$ -direction.\* Next, we recast Eq 7 in terms of angles referenced against directions  $\{\hat{r}, \hat{\theta}, \hat{z}\}$ . The *surface twist angle*,  $\psi$ , gives the azimuthal angle between the  $r$ -axis and the projection of the surface normal onto the  $r\theta$ -plane, denoted by  $\hat{n}_{r\theta}$ . The *surface tilt angle*,  $\beta$ , is the polar

\*When  $|\mathbf{v} - (\mathbf{v} \cdot \hat{z})\hat{z}|$  is zero (a sub-surface moves up or down),  $\hat{r}$  is set to the direction of the horizontal component of the surface-normal i.e.  $\hat{r} = (\hat{n} - (\hat{n} \cdot \hat{z})\hat{z}) / |\hat{n} - (\hat{n} \cdot \hat{z})\hat{z}|$ .

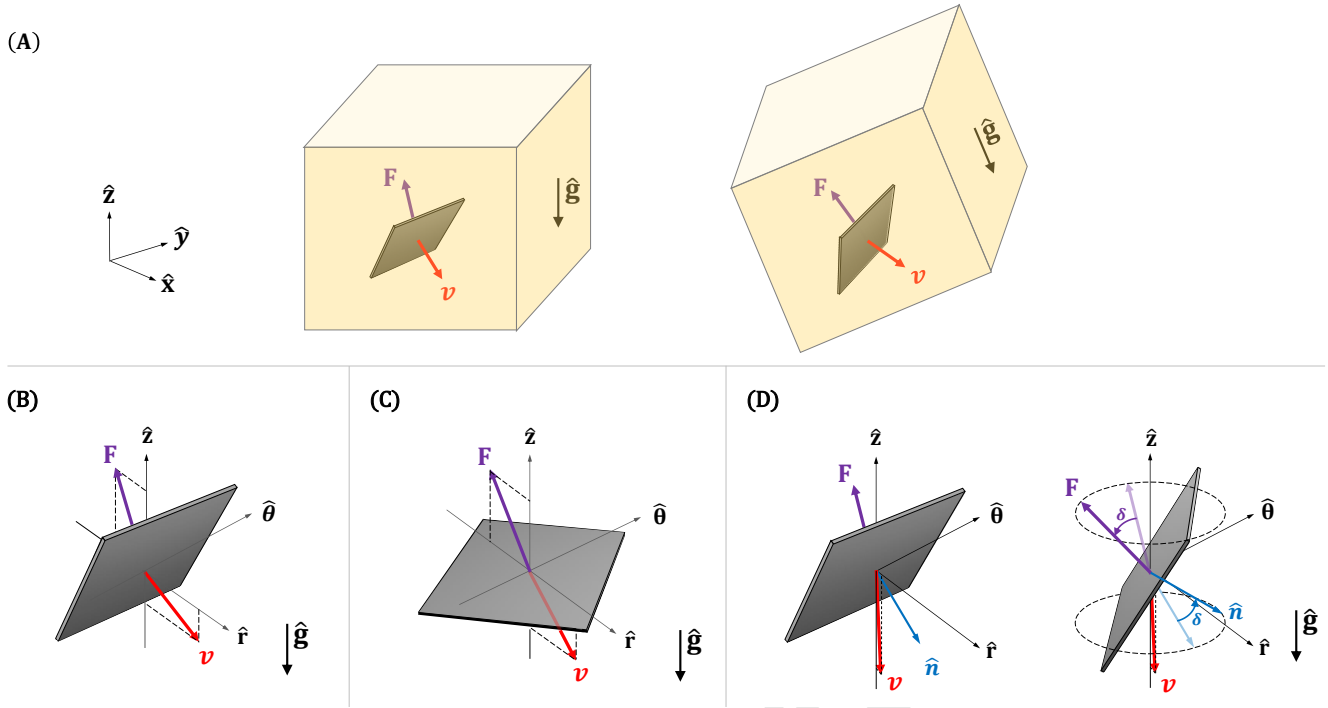


**Fig. 2.** 3D-RFT symmetry constraints: (A) Global rotational constraint requiring the drag force to be an isotropic function of the plate normal, motion direction, and gravity direction. Some consequences of this constraint are *plate twist symmetry*, *plate tilt symmetry*, and *vertical motion symmetry*. (B) A special case of *plate twist symmetry*:  $F_\theta(\beta, \gamma, \psi = 0) = 0$ . (C) A special case of *plate tilt symmetry*:  $F_\theta(\beta = 0, \gamma, \psi) = 0$ , and (D) *Vertical motion symmetry*:  $(\beta, \gamma = \pm\pi/2, \psi = 0) \rightarrow (\beta, \gamma = \pm\pi/2, \psi = \delta)$  causes  $(F_r, F_\theta = 0, F_z) \rightarrow (F_r \cos \delta, F_r \sin \delta, F_z)$ . Violet, red, and blue arrows show force, velocity, and surface-normal direction, respectively.

angle between the  $r$ -axis and the  $r\theta$ -plane. To be clear,  $\beta$  measures the angle between the  $r\theta$ -plane and one of  $\hat{n}$  or  $-\hat{n}$ , whichever gives a result in the  $[-\pi/2, \pi/2]$  range. This choice is not problematic because at any time, only one side of a plate element experiences forces, and this can be identified using the leading edge condition ( $\hat{v} \cdot \hat{n} \geq 0$ ). The local coordinate frame definitions keep the velocity vector completely within the  $rz$ -plane. Thus, once  $\{\hat{r}, \hat{\theta}, \hat{z}\}$  are determined, only one angle is needed to represent the velocity direction. This *angle of attack*,  $\gamma$ , is the angle between the velocity direction vector and the local positive  $r$ -axis. See Fig 1C for a visual representation of these angles. Based on the above definitions, the variations of each of the system characteristic angles  $\{\beta, \gamma, \psi\}$  is restricted to  $[-\pi/2, \pi/2]$  for any leading-edge surface. We use these limits in the generation of reference 3D-RFT data. Mathematical formulae for the angles in terms of vector components in a fixed cartesian frame are provided in the Section S2 of the Supplementary Information. With some algebra, one can express the  $\{\hat{n}, \hat{v}, \hat{g}\}$  basis vectors in terms of  $\{\hat{r}, \hat{\theta}, \hat{z}\}$  and the three angles (see Eq 6 of Supplementary Information). Substituting the result into Eq 7 yields the expressions for the components of  $\alpha^{\text{gen}} = \alpha_r^{\text{gen}} \hat{r} + \alpha_\theta^{\text{gen}} \hat{\theta} + \alpha_z^{\text{gen}} \hat{z}$  as follows:

$$\begin{aligned} \alpha_r^{\text{gen}}(\beta, \gamma, \psi) &= f_1 \sin \beta \cos \psi + f_2 \cos \gamma \\ \alpha_\theta^{\text{gen}}(\beta, \gamma, \psi) &= f_1 \sin \beta \sin \psi \\ \alpha_z^{\text{gen}}(\beta, \gamma, \psi) &= -f_1 \cos \beta - f_2 \sin \gamma - f_3 \end{aligned} \quad [8]$$

where  $f_i = f_i(\hat{g} \cdot \hat{v}, \hat{g} \cdot \hat{n}, \hat{n} \cdot \hat{v})$  are three as-yet undetermined functions of the three dot products, which are now given by

the three angles as follows:

$$\begin{aligned} \hat{g} \cdot \hat{v} &= \sin \gamma, & \hat{g} \cdot \hat{n} &= \cos \beta, \\ \hat{n} \cdot \hat{v} &= \cos \psi \cos \gamma \sin \beta + \sin \gamma \cos \beta. \end{aligned} \quad [9]$$

Equations 8 and 9 give the final functional form of  $\alpha^{\text{gen}}$  and the completion of the three-step process outlined in Sec 3. The 3D-RFT model we introduce is closed upon fitting the three  $f_i$  as functions of the three dot products, which we shall do in the next section using a targeted set of in-silico reference tests. Note that by building the angle dependences of  $\alpha_r^{\text{gen}}$ ,  $\alpha_\theta^{\text{gen}}$ , and  $\alpha_z^{\text{gen}}$  indirectly from the  $f_i$  using IRT rather than by directly fitting the  $\alpha^{\text{gen}}$  functions, the model is guaranteed to satisfy many easy-to-observe requirements regardless of how the  $f_i$  are picked. These include (i) ‘*plate twist symmetry*’ (Fig 2B), which requires that the sub-surface forces in the  $r$ - and  $z$ -direction should be even functions of plate twist ( $\psi$ ), and that force in the  $\theta$ -direction should be an odd function of  $\psi$ ; (ii) ‘*plate tilt symmetry*’ (Fig 2C) which requires that when the plate faces upwards or downwards ( $\beta = 0$ ), the sub-surface force in the  $\theta$ -direction should vanish, the force magnitude should depend only on  $\gamma$ , and the twist angle  $\psi$  should have no influence on the force; (iii) ‘*vertical motion symmetry*’ (Fig 2D), which requires that for any tilt  $\beta$ , as  $\gamma \rightarrow \pm\pi/2$  (approaching an upward or downward motion) any azimuthal rotation (changing  $\psi$  at constant  $\beta$ ) of a sub-surface should rotate the resultant force on the sub-surface by the same angle. Moreover, by using Eqs 8-9 we are ensured the relation for  $\alpha^{\text{gen}}$  always has the correct periodicity in the three angles.

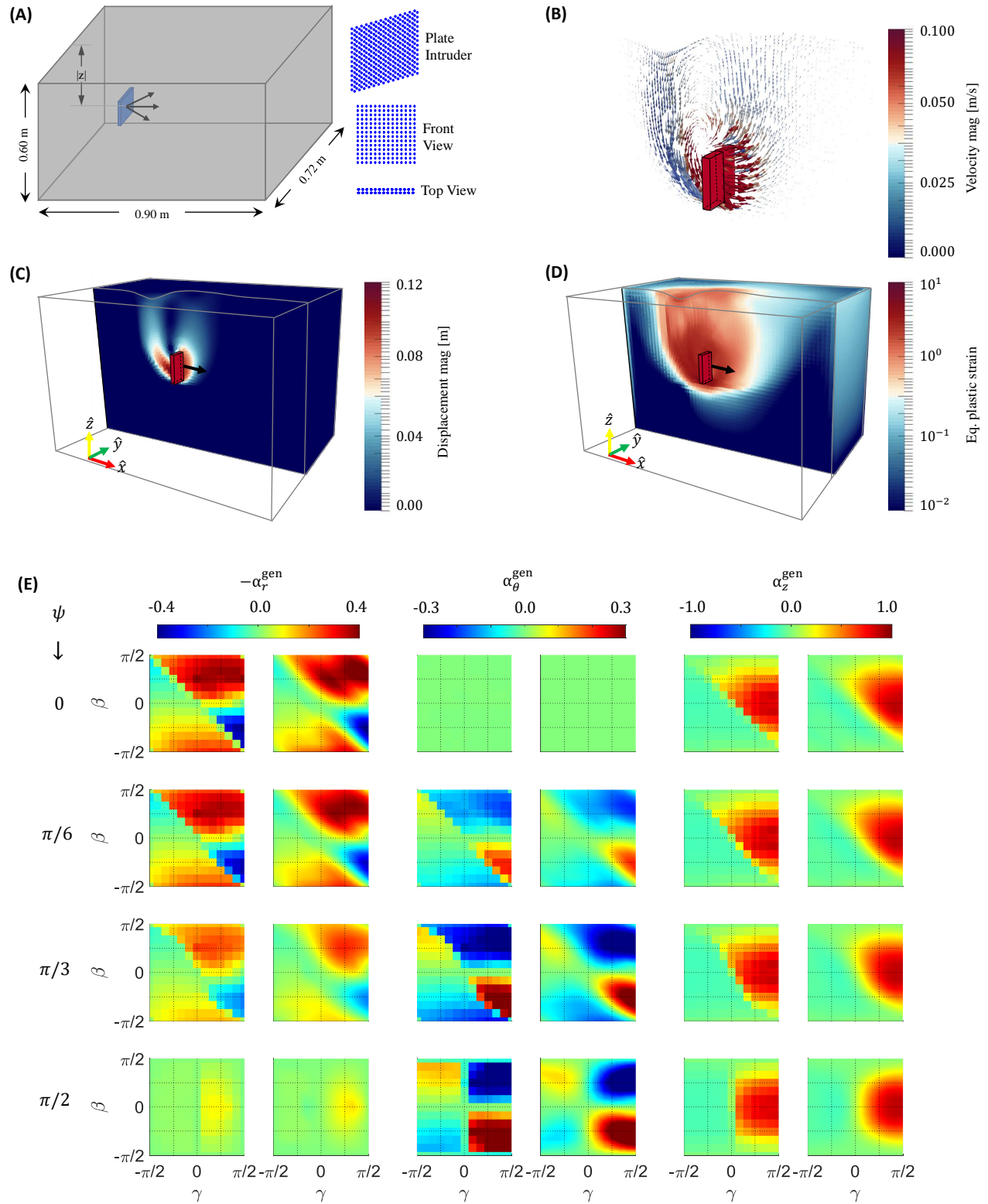


**Fig. 3. Reference data collection for 3D-RFT:** (A) We use a thin plate ( $0.105\text{m} \times 0.105\text{m} \times 0.015\text{m}$ ) intrusion setup as shown in the schematic for reference data collection for 3D-RFT. We use material point method (MPM) based continuum modeling for data collection. (B) material flow, (C) displacement magnitude, and (D) equivalent plastic strain magnitude variation from one of the test setups. Material properties are provided in the *Reference Data* section. *Sample 3D-RFT fittings:* Reference normalized forces ( $F/A|z|\xi_n$ ) and functional fittings (right) for plate intrusions at various plate twists ( $\psi = [0, \pi/6, \pi/3, \pi/2]$  rad), plate inclinations ( $\beta = -\pi/2 : \pi/6 : \pi/2$  rad), and velocity directions ( $\gamma = -\pi/2 : \pi/6 : \pi/2$  rad) for a material with  $\mu_{\text{int}} = 0.4$ ,  $\rho = 3000 \text{ kg/m}^3$ , and  $\mu_{\text{surf}} = 0.15$ . The reference data is normalized with  $\xi_n = 0.92 \times 10^6 \text{ N/m}^3$ .

## 5. Reference data

We use a large number of combinations ( $\sim 3000$ ) of material properties,  $\rho$ ,  $\mu_{\text{int}}$ , and  $\mu_{\text{surf}}$  and 3D-RFT angles  $\beta$ ,  $\gamma$ , and  $\psi$  to generate continuum modeling-based reference data for evaluating the 3D-RFT form. The details of the combinations are provided in the the Section S1 of the Supplementary Information. Polynomial fits for  $f_1$ ,  $f_2$ , and  $f_3$  are provided in the Supplementary Information (Table S3 and Table S4). Figure 3A-D shows the simulation setup used for the data collection. While both the  $\beta$  and the  $\gamma$  angles are varied over the interval  $[-\pi/2, \pi/2]$ ,  $\psi$  was varied only in  $[0, \pi/2]$  taking advantage of ‘plate twist symmetry’ discussed earlier.

Figure 3E shows an example of 3D-RFT fittings against reference data. Odd columns in the figure show the data obtained using continuum simulations as a function of  $\beta$  and  $\gamma$  at four  $\psi$  values. The material properties were  $\mu_{\text{int}} = 0.4$ ,  $\rho_c = 3000 \text{ kg/m}^3$ , and  $\mu_{\text{surf}} = 0.15$ . Corresponding 3D-RFT fittings are plotted on the even columns. We find the value of the scaling coefficient  $\xi_n$  to be  $0.92 \times 10^6 \text{ N/m}^3$  for this material. While Eq 8 represents the most generic form of 3D-RFT, the choice of the functions  $f_i$  determines the final 3D-RFT model. All the results presented in this work use 3<sup>rd</sup> degree polynomial fits for the  $f_i$  functions (Table S3). Higher-order polynomials could be used, which can better fit the reference data. We provide one such form in the Supplementary Information (Table S4). The performance of 3D-RFT does not change significantly between 3<sup>rd</sup> and 4<sup>th</sup> degree polynomial fits. The latter form fits the trends of  $|\alpha_t|/|\alpha_n|$  better but has inconsequential effects on 3D-RFT predictions for the test cases used in this study.

The 3D-RFT model we propose is completed using cubic  $\hat{f}$  fit as shown in Fig S3 — this dependence is in accord with observations of past researchers in the simpler vertical intrusion of flat plates (32) — and with  $\alpha^{\text{gen}}$  expressed using Eqs 8 in terms of third degree polynomial fits for the  $f_i$ , and using directions  $\{\hat{r}, \hat{\theta}, \hat{z}\}$  and angles  $\{\beta, \gamma, \psi\}$  as shown in Fig 3A-D. To numerically implement the model, we discretize the intruder surface into small plate elements and determine  $\{\beta, \gamma, \psi\}$  and  $\{\hat{r}, \hat{\theta}\}$  for each element. The model then provides the force on each element that is on the leading edge of the intruder. A step-by-step implementation strategy for 3D-RFT is given in the the Section S2 of the Supplementary Information.

## 6. Validation studies

We first test the accuracy of the implied localization of the proposed form of 3D-RFT (Eq 3) as well as the  $f_i$  fits by comparing predictions for ten arbitrary intruding objects to full continuum model solutions of the same intrusions. We use the continuum material properties  $\mu_{\text{int}} = 0.4$ ,  $\rho_c = 3000 \text{ kg/m}^3$ , and  $\mu_{\text{surf}} = 0.4$  for these cases. A representation of the objects and their dimensions are provided in Fig 4 and its caption. The object length scales are kept to be 7 cm in all the cases, and the objects are submerged to an initial depth of 27 cm (vertical distance between the free surface and the geometric center of the shape). The objects are moved at a speed of 0.1 m/s in different directions in the  $xz$ -plane. These directions are characterized using  $\theta$ , which represents the angle between the velocity direction ( $\hat{v}_\theta$ ) and the positive  $x$ -axis in a clockwise direction (same as  $\gamma$  definition for a plate element). Negative  $\theta$  represents upward motion, positive  $\theta$  represents downward motion, and  $\theta = 0$  represents horizontal

motion along the  $x$ -direction. The variations of net-force ( $F_x$ ,  $F_y$ , and  $F_z$ ) with  $\theta$  are plotted in Fig 4. 3D-RFT agrees with the continuum solutions well in modeling all the intrusion test scenarios considered in Fig 4. Objects with sharp corners generally show somewhat weaker fits than those with smoother shapes; this could be because sharp corners are difficult to represent with our material point method.

**Validation of 3D-RFT with detailed DEM studies.** We further check the performance of 3D-RFT with two DEM studies. In these studies, we measure net moment, net force, and resistive force distribution on bodies intruding into granular volumes with simultaneous rotation and translation velocities. We use a 50/50 mixture of 3 mm and 3.4 mm diameter ( $d$ ) grains with a grain density of  $2470 \text{ kg/m}^3$  and the granular volumes have an effective bulk density of  $1310 \text{ kg/m}^3$  ( $\phi \approx 0.53$ ) in both the DEM studies. We determine the internal coefficient of friction  $\mu_{\text{int}}$  as 0.21 using simple shear simulations. Section S8 of the Supplementary Information provides more details of the simple shear test setup and detailed material properties. Using this value together with the known  $\hat{f}$  relationship, We obtain a scaling coefficient ( $\xi_n$ ) value of  $0.12 \times 10^6 \text{ N/m}^3$ . See Table S1 and Sec S4 for more details.

*Cylinder Drill:* In this test, we model simultaneous rotation and translation (drilling) of a *solid cylindrical* intruder along the  $z$ -axis in a granular volume (diameter= 0.05 m, length=0.14 m). The setup consists of approximately  $6 \times 10^5$  particles in a  $100d \times 100d \times 70d$  sized granular bed. The setup dimensions and setup schematic are provided in Fig 5. The figure also shows the variations of force and moment on the intruder over time from the DEM studies versus 3D-RFT. In addition, the figure shows the variation of stress over the intruder surface from DEM and 3D-RFT. All reported components (net force and moments, as well as stress distributions) show a strong match between the two approaches.

*Bunny Drill:* In this test, we model the drilling motion ( $\omega = 2\pi \text{ rad/s}$ ,  $v = 0.1 \text{ m/s}$ ) of a *Stanford Bunny* (34) shaped rigid intruder in a granular volume. The shape is chosen because it is an example of a complex, asymmetric 3D object. The granular bed consists of approximately  $2.1 \times 10^6$  particles spread over a  $150d \times 150d \times 88d$  sized domain. The bunny shape was slightly modified from the standard shape — the shape was proportionally scaled in such a way that the bunny height measures 0.1 m, and the bunny base was flattened to make the base a plane surface without an inward extrusion. Figure 6 shows the simulation setup where the grains are colored with velocity magnitudes. Figure 6 also shows the variation of stresses over the intruder surface from DEM and 3D-RFT. All the reported components (net force and moments, as well as stress distributions) show a strong match between the two approaches.

## 7. Conclusion

This work proposes a mechanistic framework for developing reduced-order models in soft-materials. Successful development of a granular 3D-RFT that overcomes the limitations of previous attempts in this direction (see Sec 1 of Supplemental 27 Information) indicates the robustness of the approach for

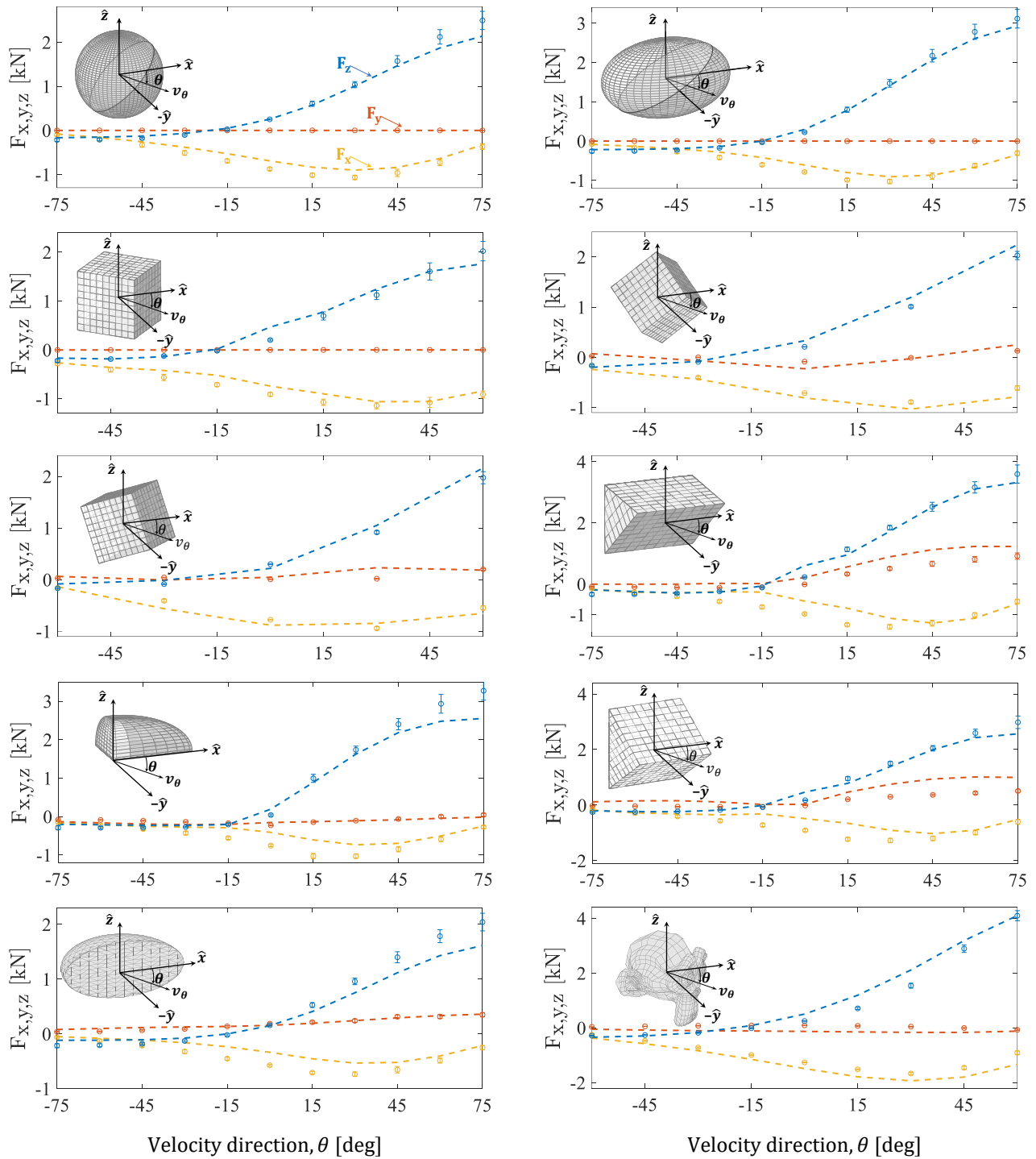


**Fig. 4. 3D-RFT Verification Studies 1-10:** Variation of different force components ( $F_x$ : yellow,  $F_y$ : orange, and  $F_z$ : blue) during motions of various rigid objects (intruders) obtained from continuum modeling ('o' markers) and 3D-RFT (dashed lines) at various velocity directions ( $\hat{v}_\theta$ ). All the studies were conducted at a velocity magnitude of 0.1 m/s.  $\theta$  represents the angle between  $\hat{v}_\theta$  and the positive x-axis. All the velocities completely lie in the  $xz$ -plane. A pictorial representation of each intruder is provided in the corresponding sub-figure. The intruder shapes include (1) a 5 cm radius sphere, (2) an ellipsoid with [7.5, 4.5, 4.5] cm semi-axes ( $x, y, z$ ), (3) a 7.5 cm tilted cube, rotated from a cartesian alignment by  $\pi/4$  radians about the  $z$ -axis, (4) a 7.5 cm cube sequentially rotated by  $\pi/3$  and  $\pi/4$  radians along the  $y$ -axis and  $z$ -axis from a cartesian alignment, (5) a 7.5 cm cube sequentially rotated by  $\pi/6$  and  $\pi/3$  radians along the  $y$ -axis and  $z$ -axis from a cartesian coordinate alignment, (6) an isosceles right angle prism with 7.5 cm equal sides and 10.5 cm width, (7) a quarter ellipsoid with [7.5, 4.5, 4.5] cm semi-axes ( $x, y, z$ ) ( $x > 0$  and  $y > 0$ ), (8) an isosceles right angle prism with equal sides of 10.5 cm and 7.5 cm width, (9) a half-ellipsoid with [7.5, 4.5, 4.5] cm semi-axes ( $x, y, z$ ) ( $y > 0$ ), and (10) a monkey head shape from the open-source 3D computer graphics software 'Blender' at a scale factor of 0.075 and facing  $\pi/4$  radians from the positive  $x$ -direction in the  $xy$ -plane.

these purposes. The 3D-RFT developed herein is an important step towards developing a generic real-time modeling technique

capable of modeling granular intrusion of arbitrarily shaped objects over a large range of low and high-speed scenarios in di-

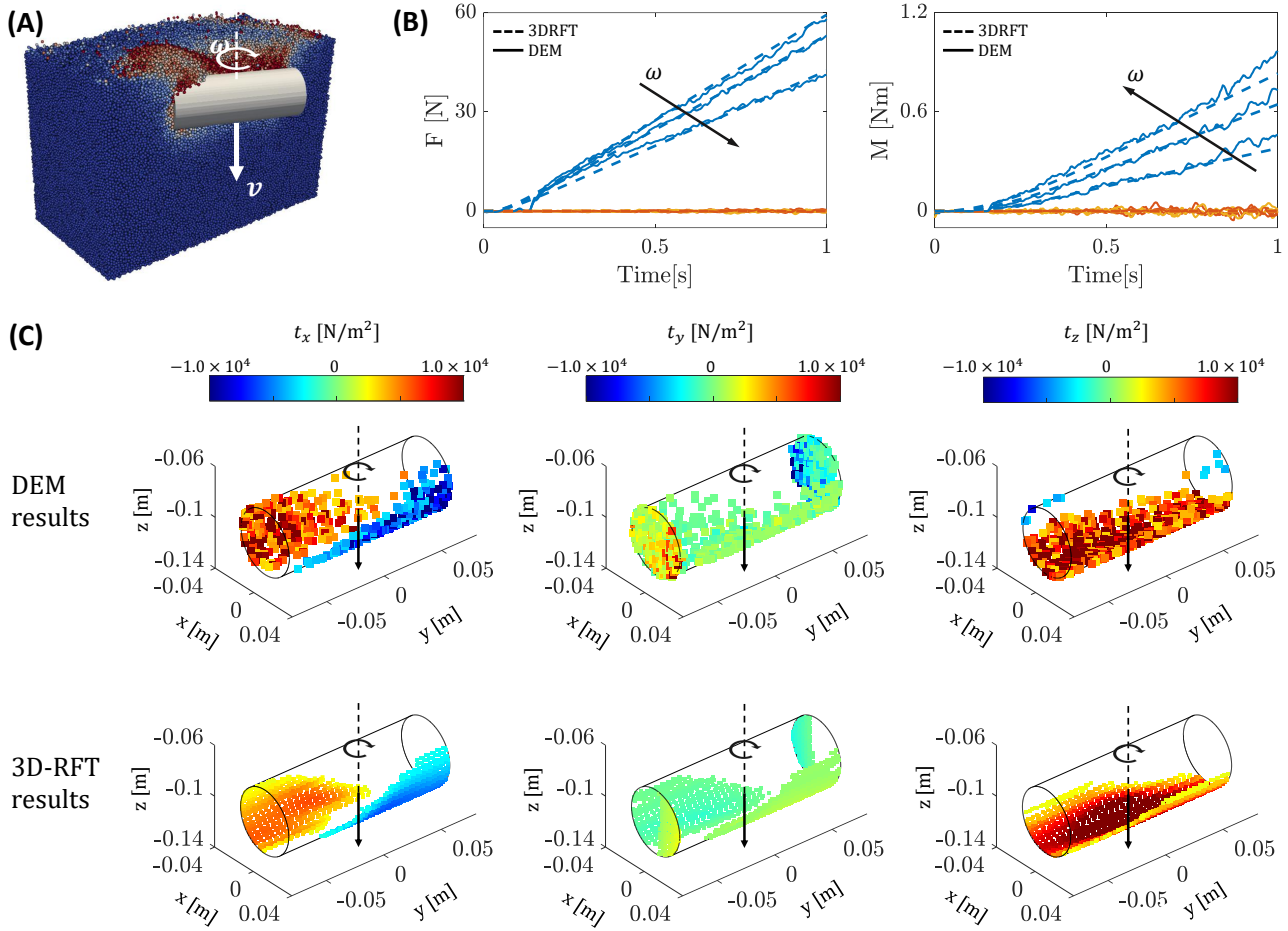


**Fig. 5.** DEM based 3D-RFT verification: Cylinder drill: (A) A snapshot of the cylinder drill setup where a 50 mm diameter and 140 mm length cylinder was simultaneously rotated ( $\omega$ , clockwise) and translated ( $v$ , downwards) along the  $z$ -axis. We use three combinations of  $(\omega, v)$ :  $[(0.25\pi, 0.1), (0.5\pi, 0.1), (\pi, 0.1)]$  (rad/s,m/s). Black arrows in (B) show the direction of increasing  $\omega$  in each graph. The grains are colored with velocity magnitudes. The simulation domain consisted  $\sim 6 \times 10^5$  particles (50/50 mix of 3 mm and 3.4 mm diameter ( $d$ ) grains) spread over  $100d \times 100d \times 70d$  physical space. (B) Variation of net force ( $F$ , left) and moment ( $M$ , right) components ( $x$ : yellow,  $y$ : orange, and  $z$ : blue) from DEM (solid lines) and 3D-RFT (dotted lines) for  $\omega = \pi$  rad/s. (C) Variation of various force components from DEM (Top) and 3D-RFT (Bottom) at a 10 cm depth below the free surface ( $t = 1$  s). The DEM material properties are provided in table S2 of the Supplementary Information.

verse materials and environments. Previously, granular RFT's usage has focused on the modeling of arbitrary 2D objects moving in-plane. We have proposed an extension of RFT to three dimensions in a fashion consistent with granular continuum mechanics and necessary symmetry constraints. The accuracy of the proposed 3D-RFT was demonstrated against a variety of full-field intrusion simulations, both continuum and DEM. Notably, we provide a scheme that determines 3D-RFT in different intrusion systems quickly and directly in terms of basic properties of the granular media ( $\rho_c$  and  $\mu_{\text{int}}$ ) and the intruder surface ( $\mu_{\text{surf}}$ ). The most immediate opportunity to expand 3D-RFT would be to combine 3D-RFT with Dynamic RFT (25) to build a high-speed three-dimensional RFT (3D-DRFT). The current form of 3D-RFT does not include a "shadowing effect" i.e. the fact that forces are reduced on leading edge surfaces that lie in the immediate wake behind another part of the intruder (35). Such effects are more pronounced in intruders with complex shapes or fine geometric features such as the Bunny shape we consider in this study. Characterizing this effect would be an important addition to RFT. Effects

of multibody intrusions (24, 36), density variations (37), inertial and non-inertial velocity effects (3, 25, 38), cohesion (39, 40), and inclined domains (41) on the resistive forces experienced by intruding bodies are among other aspects for further exploration toward the ultimate goal of a generic and fast granular intrusion model applicable to terradynamical motions (8), granular impact systems (42, 43), locomotors (44), and many other similar applications. As a reminder, the mechanistic approach that produced 3D-RFT has clear future extensions to other materials including cohesive media and many non-Newtonian fluids (such as Herschel-Bulkley fluids), where the basic program involving continuum-level arguments and symmetry constraints can also be exploited to produce physically-motivated reduced-order models.

## Materials and Methods

**Evaluation of quasi-static conditions in a system .** We use the following definitions of the micro-inertial number  $I$  and the macro-inertial number  $I_{\text{mac}}$  for evaluating the applicability of 3D-RFT in modeling

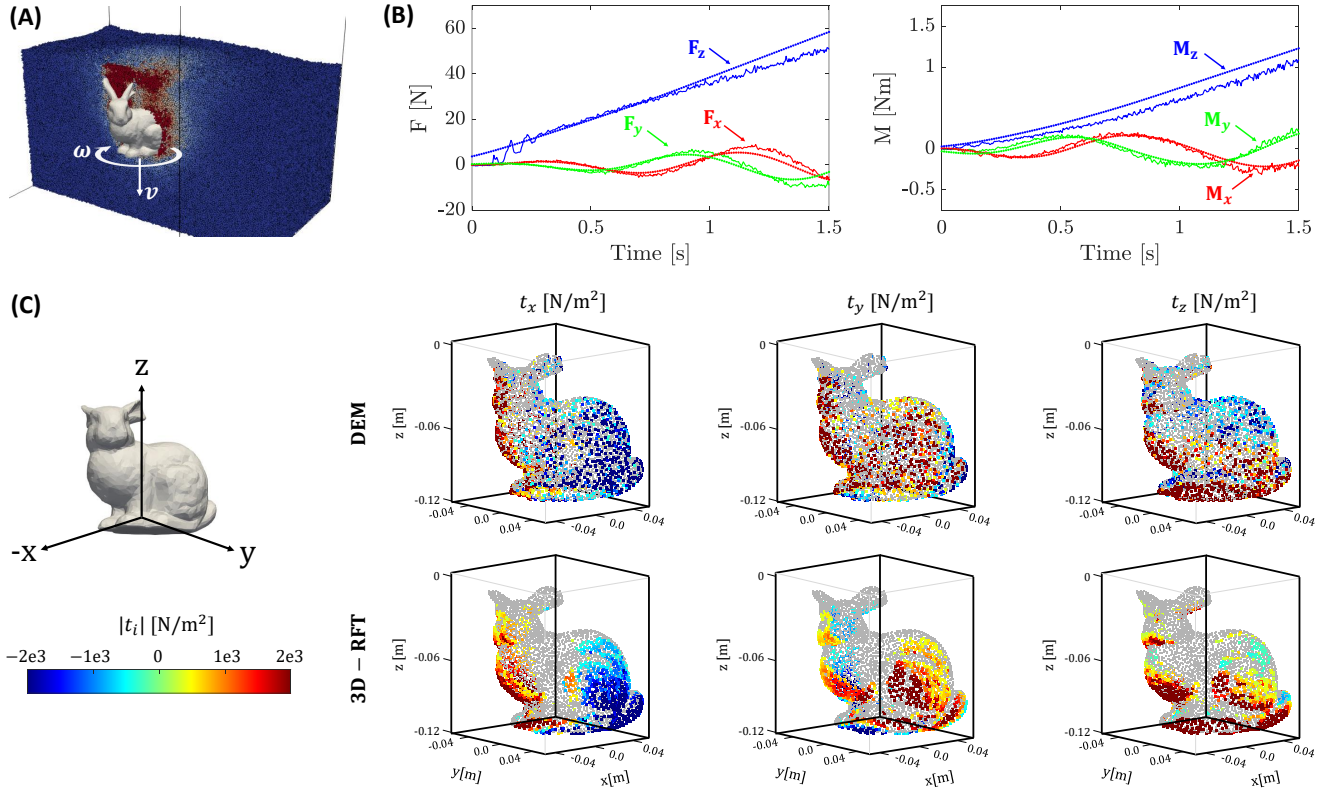


**Fig. 6.** DEM based 3D-RFT verification: Bunny drill: (A) A snapshot of the Stanford-Bunny drill setup where a 10 cm high stanford-bunny was simultaneously rotated ( $\omega = 2\pi$  rad/s, clockwise) and translated ( $v = 0.1$  m/s, downwards) along the  $z$ -axis. The grains are colored with velocity magnitudes. The simulation domain consisted of  $\sim 2.1 \times 10^6$  particles (50/50 split of 3 mm and 3.4 mm diameter ( $d$ ) grains) spread over a  $150d \times 150d \times 88d$  physical space. (B) Variation of net force ( $F$ , left) and moment ( $M$ , right) components ( $x$ : yellow,  $y$ : orange, and  $z$ : blue) from DEM (solid lines) and 3D-RFT (dotted lines). (C) Components of the surface stress distribution from DEM (Top) and 3D-RFT (Bottom) at a 5 cm bunny-center-depth below the free surface. The DEM material properties are provided in Table S2 of the Supplementary Information.

the granular resistive forces in a granular intrusion system;

$$I = \dot{\gamma} / \sqrt{P/\rho_g d^2}, \quad I_{\text{mac}} = v / \sqrt{P/\rho_g},$$

where  $\dot{\gamma}$  represents the material shear rate,  $P$  represents the hydrostatic pressure,  $\rho_g$  represents the material grain density,  $d$  represents the mean grain diameter, and  $v$  represents the speed. The  $I_{\text{mac}}$  formulation is equivalent to the inverse square root of the *Euler number* which measures the ratio of the dynamic pressure  $\rho v^2$  to the total pressure  $P$ .

The macro- and micro-inertial numbers are defined pointwise within a granular media so, to determine if an intrusion is quasi-static, it is convenient to determine characteristic values for these numbers. For this, we use characteristic values of  $\dot{\gamma}$ ,  $P$ , and  $v$ . We assume that the intruder has an angular velocity  $\omega$ , a translational velocity  $v_{\text{intruder}}$ , and a characteristic length  $L$ . We also assume that the media has a critical density  $\rho_c$  and that the system is acted upon by gravity  $g$ . We characterize  $v$  as  $v = \max(v_{\text{intruder}}, L\omega/2)$  and  $\dot{\gamma}$  as  $\dot{\gamma} = v/L$ . We consider intrusive loading of the system at characteristic depth  $L$  to give a characteristic  $P$  as  $\xi_n L$ . Upon substitution, we get:

$$I \sim (v/L) / \sqrt{(\xi_n L) / \rho_g d^2} = \sqrt{\frac{v^2 \rho_g d^2}{\xi_n L^3}} = \frac{vd}{L} \sqrt{\frac{\rho_g}{\xi_n L}},$$

$$I_{\text{mac}} \sim v / \sqrt{\xi_n L / \rho_g} = v \sqrt{\frac{\rho_g}{\xi_n L}}.$$

From the above equations, we observe that the characteristic value of  $I_{\text{mac}}$  reduces to a multiple of the *Froude number* ( $Fr$ ) in gravity loaded systems. To this end, Sunday et al. (45) explored the existence of macro-inertial effects during high-speed granular intrusions and observed insignificant contributions of macro-inertial effects in the material force response for  $Fr < 1.5$ , which gives

$I_{\text{mac}} \lesssim 0.48$ . Similarly, Agarwal et al. (25), observed insignificant macro-inertial effects (macro-inertial forces  $< 10\%$  of static resistive forces i.e.  $\rho A v^2 / K|z| < 10\%$ ) in granular plate intrusions at  $I_{\text{mac}} < 0.16$ . Thus, we impose an upper limit of 0.15 on  $I_{\text{mac}}$  to be quasi-static. The amount  $I$  affects the flow can be quantified by how much it changes the apparent internal friction (46, 47). To keep these changes bounded by 10% we set an upper bound on the characteristic value of  $I$  to be 0.010 so as to ensure quasi-static conditions. For all the test cases used in this study, we choose system parameters in such a way that  $I$  and  $I_{\text{mac}}$  are always below above mentioned limits keeping their motions in quasi-static limits. The test cases 1-10 are continuum simulation that use a rate-independent constitutive law and have  $I_{\text{mac}} \sim 0.02$  ( $L \approx 0.07$  m,  $v = 0.1$  m/s,  $\xi_n = 0.92 \times 10^6$ ,  $\rho_c = 3000$  kg/m<sup>3</sup>). In the DEM based cylinder drill test cases, we find  $I < 0.002$  and  $I_{\text{mac}} < 0.07$  ( $L \approx 0.10$  m,  $\omega < \pi$  rad/s,  $v_{\text{intruder}} = 0.1$  m/s,  $\xi_n = 0.12 \times 10^6$ ,  $\rho_g = 2470$  kg/m<sup>3</sup>). Similarly, in the bunny drill test case, we find  $I \approx 0.004$  and  $I_{\text{mac}} \sim 0.13$  ( $L \approx 0.10$  m,  $\omega = 2\pi$  rad/s,  $v_{\text{intruder}} = 0.1$  m/s,  $\xi_n = 0.12 \times 10^6$ ,  $\rho_g = 2470$  kg/m<sup>3</sup>). Thus, 3D-RFT is a valid approach for modeling all the test cases considered in this study, based on the insignificance of micro- and macro- inertial force contributions.

**Continuum approach accuracy validation.** Several studies in the past have verified the accuracy of this constitutive formulation in plane-strain problems. We use the 3D numerical implementation of MPM developed by Baumgarten and Kamrin (29) for this study which has been successfully used for modeling complex problems in the past (29, 30). For the continuum model to be useful to determine input data for a 3D-RFT, it must be shown to reliably match experiments for 3D plate intrusions. We test this in two scenarios.

In the first test case, we check if the 3D-continuum simulations can regenerate the experimental variation of force/depth/area on

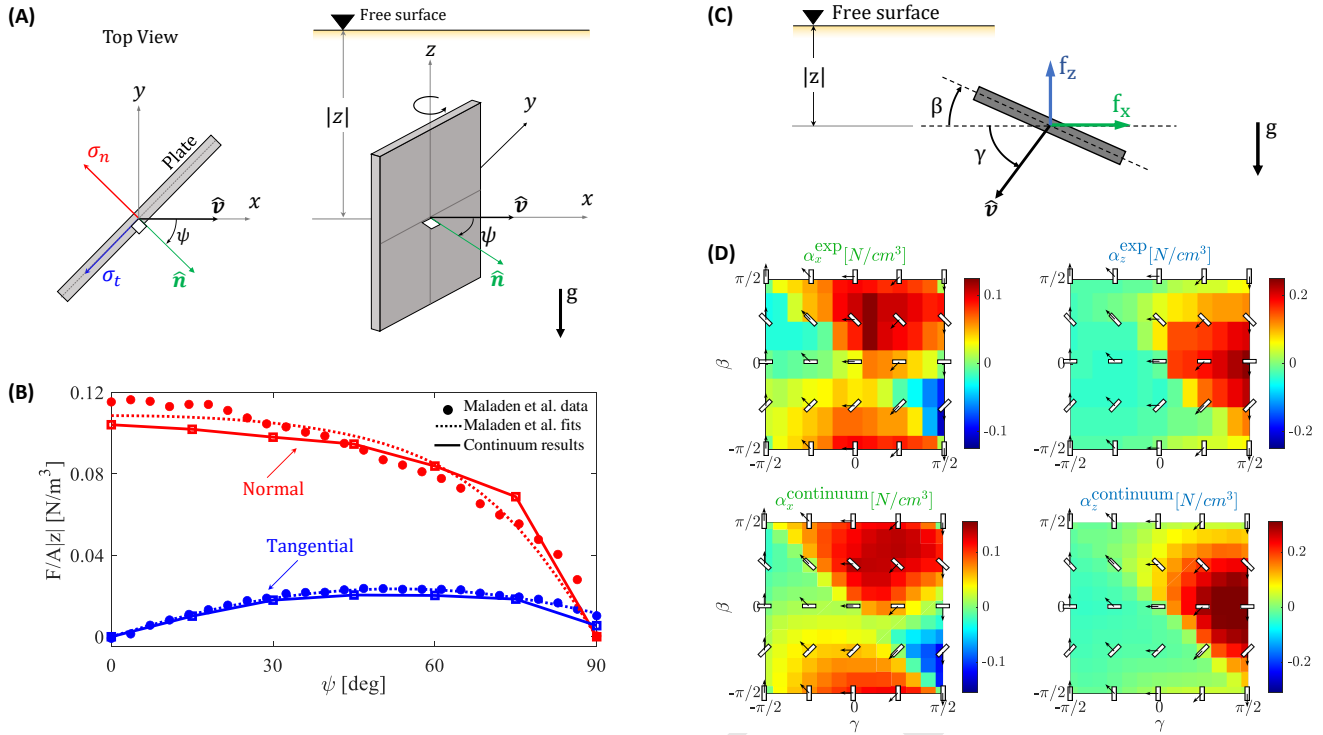


**Fig. 7. Experiment vs Continuum Model — Dependence on twist angle:** (A) Schematic of plate orientations, and (B) variations of normal (red) and tangential (blue) forces from Maladen et al (48) experiments (● marker), their analytical fits to their results (dotted lines), and continuum simulations (■ marker with solid line). The forces are normalized by the plate center-depth ( $|z|$ ) and plate area. Experiments (loosely packed 3 mm glass particles) as well as simulation use glass beads ( $\rho_g = 2500 \text{ kg/m}^3$  and  $\rho_c = 0.6$ ) as the granular media. Continuum simulations use  $\mu_{\text{int}} = 0.4$  and  $\mu_{\text{surf}} = 0.27$  in accordance with reported experimental values. The original Maladen et al. (48) results used a twist angle ( $\beta_d = \pi/2 - \psi$ ) as the  $x$ -axis in their plots. We have modified the plots to have  $\psi = \pi/2 - \beta_d$  on  $x$ -axis for simplifying the discussion. — *Comparison of in-plane plate motions:* (C) Schematic of plate orientation angle  $\beta$  and  $\gamma$  for in-plane motion study conducted using 3D simulation setup shown in figure 3A-D. (D) Force/area/depth ( $\alpha$ ) from Li et al.(14) experiments (top) and continuum simulations (bottom). The plate configurations are also overlaid on graphs for clarity. The plates had no twist ( $\psi = 0$ ) in regards to 3D-RFT definitions in these tests. Both the experiments and the simulations use glass beads with grain density ( $\rho_g$ ) of  $2500 \text{ kg/m}^3$  and a packing fraction ( $\phi_c$ ) of 0.58. Internal friction is  $\mu_{\text{int}} = 0.4$  and surface friction,  $\mu_{\text{surf}} = 0.4$  for continuum simulations to match reported values in Li et al.(14).

flat plates in submerged granular beds from Li et al.(14). This experimental data was also used by Li et al.(14) in the generation of 2D-RFT form. We use an effective materials density of  $\rho_c = 1450 \text{ kg/m}^3$  (loose glass beads,  $\rho_g = 2500 \text{ kg/m}^3$ ,  $\phi_c = 0.58$ ) inline with Li et al.(14) experiments and an approximate internal friction value for glass beads as  $\mu_{\text{int}} = 0.4$ . The media-plate surface friction was taken as  $\mu_{\text{surf}} = 0.4$ . The relative values of the forces from continuum results remarkably match the experimental observations. The absolute values from continuum results, however, are higher than experiments by a constant multiplicative factor of  $\sim 1.1$ . A smaller value of  $\mu_{\text{int}}$  for glass beads could have provided a closer match to the experiments as the graphs are not expected to change their shape with changing internal friction values (14). But we do not attempt the exact calibration as the purpose of the test was to verify the accuracy of the continuum formulation and implementation. These results establish sufficient efficacy of the continuum model for plate motions in which the velocity, plate normal, and gravity or co-planar.

In the second test case, we assess the quantitative accuracy of the continuum approach in modeling in-plane as well as out-of-plane forces. We consider a study Maladen et al.(48) which measured the normal and tangential forces on submerged plates moving horizontally in granular media as a function of plate twist (see Fig 7 (top) for angles definition). The material properties are provided in the figure caption. The continuum results match observations from Maladen et al.(48) well.

The combination of the above two studies establishes the overall accuracy of the continuum model and its implementation for both in-plane and out-of-plane inputs and outputs in plate intrusion problems.

**ACKNOWLEDGMENTS.** SA, and KK acknowledge support from Army Research Office (ARO) grants W911NF1510196 and W911NF1810118 and support from the U.S. Army Tank-Automotive Research, Development and Engineering Center (TARDEC). DG acknowledges support from ARO grant W911NF-18-1-0120. SA thanks Aaron Baumgarten, who provided the authors with his 3D-MPM model implementation. We also thank Andras Karsai for helpful discussions on potential forms of 3D-RFT.

1. Sigurdur T Thoroddsen and Amy Q Shen. Granular jets. *Physics of Fluids*, 13(1):4–6, 2001.
2. Shashank Agarwal, Carmine Senatore, Tingnan Zhang, Mark Kingsbury, Karl Iagnemma, Daniel I Goldman, and Ken Kamrin. Modeling of the interaction of rigid wheels with dry granular media. *Journal of Terramechanics*, 85:1–14, 2019.
3. Perrin E Schiebel, Henry C Astley, Jennifer M Rieser, Shashank Agarwal, Christian Hubicki, Alex M Hubbard, Kelimar Diaz, Joseph R Mendelson III, Ken Kamrin, and Daniel I Goldman. Mitigating memory effects during undulatory locomotion on hysteretic materials. *Elife*, 9:e51412, 2020.
4. Natalia Artemieva and Boris Ivanov. Launch of martian meteorites in oblique impacts. *Icarus*, 171(1):84–101, 2004.
5. Laura K Treers, Cyndia Cao, and Hannah S Stuart. Granular resistive force theory implementation for three-dimensional trajectories. *IEEE Robotics and Automation Letters*, 6(2):1887–1894, 2021.
6. Auke J Ijspeert. Biorobotics: Using robots to emulate and investigate agile locomotion. *science*, 346(6206):196–203, 2014.
7. Devaraj Van Der Meer. Impact on granular beds. *Annual review of fluid mechanics*, 49:463–484, 2017.
8. Rui He, Corina Sandu, Aamir K Khan, A Glenn Guthrie, P Schalk Els, and Herman A Hamersma. Review of terramechanics models and their applicability to real-time applications. *Journal of Terramechanics*, 81:3–22, 2019.
9. Mieczyslaw Gregory Bekker. Introduction to terrain-vehicle systems. *University of Michigan Press*, 1969.
10. Jo-Yung Wong and AR Reece. Prediction of rigid wheel performance based on the analysis of soil-wheel stresses part i. performance of driven rigid wheels. *Journal of Terramechanics*, 4(1):81–98, 1967.
11. Hans B Pacejka and Egbert Bakker. The magic formula tyre model. *Vehicle system dynamics*,

- 21(S1):1–18, 1992.
12. James Gray and GJ Hancock. The propulsion of sea-urchin spermatozoa. *Journal of Experimental Biology*, 32(4):802–814, 1955.
  13. Charles J Brokaw. Flagellar propulsion. *Journal of Experimental Biology*, 209(6):985–986, 2006.
  14. Chen Li, Tingnan Zhang, and Daniel I Goldman. A terradynamics of legged locomotion on granular media. *science*, 339(6126):1408–1412, 2013.
  15. Lei Huang, Junda Zhu, Yufeng Yuan, and Yh Yin. A dynamic resistive force model for designing mobile robot in granular media. *IEEE Robotics and Automation Letters*, 2022.
  16. Ryan D Maladen, Yang Ding, Chen Li, and Daniel I Goldman. Undulatory swimming in sand: subsurface locomotion of the sandfish lizard. *science*, 325(5938):314–318, 2009.
  17. Tingnan Zhang and Daniel I Goldman. The effectiveness of resistive force theory in granular locomotion. *Physics of Fluids*, 26(10):101308, 2014.
  18. Pierre Jop, Yoël Forterre, and Olivier Pouliquen. A constitutive law for dense granular flows. *Nature*, 441(7094):727, 2006.
  19. GDR MiDi. On dense granular flows. *The European Physical Journal E*, 14(4):341–365, 2004.
  20. Nick Gravish, Paul B. Umbanhowar, and Daniel I. Goldman. Force and flow at the onset of drag in plowed granular media. *Physical Review E*, 89(4), apr 2014. .
  21. Hesam Askari and Ken Kamrin. Intrusion rheology in grains and other flowable materials. *Nature materials*, 15(12):1274, 2016.
  22. Sachith Dunatunga and Ken Kamrin. Continuum modelling and simulation of granular flows through their many phases. *Journal of Fluid Mechanics*, 779:483–513, 2015.
  23. Sachith Dunatunga and Ken Kamrin. Continuum modeling of projectile impact and penetration in dry granular media. *Journal of the Mechanics and Physics of Solids*, 100:45–60, 2017.
  24. Shashank Agarwal, Andras Karsai, Daniel I Goldman, and Ken Kamrin. Efficacy of simple continuum models for diverse granular intrusions. *Soft Matter*, 17(30):7196–7209, 2021.
  25. Shashank Agarwal, Andras Karsai, Daniel I Goldman, and Ken Kamrin. Surprising simplicity in the modeling of dynamic granular intrusion. *Science Advances*, 7(17):eabe0631, 2021.
  26. Shashank Agarwal et al. Development of a reduced-order modeling technique for granular locomotion. Master's thesis, Massachusetts Institute of Technology, 2019.
  27. James Slonaker, D Carrington Motley, Qiong Zhang, Stephen Townsend, Carmine Senatore, Karl Iagnemma, and Ken Kamrin. General scaling relations for locomotion in granular media. *Physical Review E*, 95(5):052901, 2017.
  28. Qiong Zhang, Stephen Townsend, and Ken Kamrin. Expanded scaling relations for locomotion in sloped or cohesive granular beds. *Physical Review Fluids*, 5(11):114301, 2020.
  29. Aaron S Baumgarten and Ken Kamrin. A general fluid–sediment mixture model and constitutive theory validated in many flow regimes. *Journal of Fluid Mechanics*, 861:721–764, 2019.
  30. Aaron S Baumgarten and Ken Kamrin. A general constitutive model for dense, fine-particle suspensions validated in many geometries. *Proceedings of the National Academy of Sciences*, 116(42):20828–20836, 2019.
  31. François Guillard, Yoël Forterre, and Olivier Pouliquen. Lift forces in granular media. *Physics of Fluids*, 26(4):043301, 2014.
  32. Wenting Kang, Yajie Feng, Caishan Liu, and Raphael Blumenfeld. Archimedes' law explains penetration of solids into granular media. *Nature communications*, 9(1):1–9, 2018.
  33. GF Smith. On isotropic functions of symmetric tensors, skew-symmetric tensors and vectors. *International journal of engineering science*, 9(10):899–916, 1971.
  34. Greg Turk and Marc Levoy. Zippered polygon meshes from range images. In *Proceedings of the 21st annual conference on Computer graphics and interactive techniques*, pages 311–318, 1994.
  35. Hirotaka Suzuki, Kota Katsushima, and Shingo Ozaki. Study on applicability of rft to traveling analysis of wheel with grousers: Comparison with dem analysis as a virtual test. *Journal of Terramechanics*, 83:15–24, 2019.
  36. Swapnil Pravin, Brian Chang, Endao Han, Lionel London, Daniel I Goldman, Heinrich M Jaeger, and S Tonia Hsieh. Effect of two parallel intruders on total work during granular penetrations. *Physical Review E*, 104(2):024902, 2021.
  37. Nick Gravish, Paul B Umbanhowar, and Daniel I Goldman. Force and flow transition in plowed granular media. *Physical review letters*, 105(12):128301, 2010.
  38. Hiroaki Katsuragi and Douglas J Durian. Unified force law for granular impact cratering. *Nature Physics*, 3(6):420, 2007.
  39. Alex A Francoeur and Kelly M Dorgan. Burrowing behavior in mud and sand of morphologically divergent polychaete species (annelida: Orbiniidae). *The Biological Bulletin*, 226(2): 131–145, 2014.
  40. Shivakumar Athani and Pierre Rognon. Pulling objects out of cohesive granular materials. *Granular Matter*, 23(3):1–10, 2021.
  41. Antoine Humeau, Miguel Piñeira, Jérôme Crassous, and Jérôme Casas. Locomotion of ants walking up slippery slopes of granular materials. *Integrative Organismal Biology*, 1(1): obz020, 2019.
  42. AS Soliman, SR Reid, and W Johnson. The effect of spherical projectile speed in ricochet off water and sand. *International Journal of Mechanical Sciences*, 18(6):279–in2, 1976.
  43. Esteban Wright, Alice C Quillen, Juliana South, Randal C Nelson, Paul Sánchez, John Siu, Hesam Askari, Miki Nakajima, and Stephen R Schwartz. Ricochets on asteroids: Experimental study of low velocity grazing impacts into granular media. *Icarus*, 351:113963, 2020.
  44. Henry C Astley, Joseph R Mendelson III, Jin Dai, Chaohui Gong, Baxi Chong, Jennifer M Rieser, Perrin E Schiebel, Sarah S Sharpe, Ross L Hatton, Howie Choset, et al. Surprising simplicities and syntheses in limbless self-propulsion in sand. *Journal of Experimental Biology*, 223(5):jeb103564, 2020.
  45. Cecily Sunday, Naomi Murdoch, Arnaud Wilhelm, Melanie Drilleau, Yun Zhang, Simon Tardivel, and Patrick Michel. The influence of gravity on granular impacts-ii. a gravity-scaled collision model for slow interactions. *Astronomy & Astrophysics*, 658:A118, 2022.
  46. GDR MiDi gdrmidi@polytech. univ-mrs. fr http://www.lmgc. univ-montp2. fr/MiDi/. On dense granular flows. *The European Physical Journal E*, 14:341–365, 2004.
  47. Frédéric Da Cruz, Sacha Emam, Michaël Prochnow, Jean-Noël Roux, and François Chevoir. Rheophysics of dense granular materials: Discrete simulation of plane shear flows. *Physical Review E*, 72(2):021309, 2005.
  48. Ryan D Maladen, Yang Ding, Paul B Umbanhowar, Adam Kamor, and Daniel I Goldman. Mechanical models of sandfish locomotion reveal principles of high performance subsurface sand-swimming. *Journal of The Royal Society Interface*, 8(62):1332–1345, 2011.